

Multi-wavelength probes of the Milky Way’s Cold Interstellar Medium: Radio H_I and Optical K_I Absorption with GASKAP and GALAH

Hiep Nguyen¹*, Sven Budер^{1,2}, Juan D. Soler³, N. M. McClure-Griffiths¹, J. R. Dawson^{4,5,5}, James Dempsey^{1,5}, Helga Dénes⁵, John M. Dickey⁵, Ian Kemp⁵, Denis Leahy⁵, Callum Lynn¹, Yik Ki Ma⁵, Antoine Marchal¹, Eric Muller¹, Gyueun Park⁵, Nickolas M. Pingel⁵, Jacco Th. van Loon¹

¹Research School of Astronomy and Astrophysics, The Australian National University, Canberra, ACT 2611, Australia

²ARC Centre of Excellence for All Sky Astrophysics in 3 Dimensions (ASTRO 3D), Australia

³Istituto di Astrofisica e Planetologia Spaziali (IAPS). INAF. Via Fosso del Cavaliere 100, 00133 Roma, Italy

⁴CSIRO Information Management and Technology, GPO Box 1700 Canberra, ACT 2601, Australia

⁵School of Natural Sciences, Private Bag 37, University of Tasmania, Hobart, TAS, 7001, Australia

⁵Korea Astronomy and Space Science Institute, 776 Daedeok-daero, Daejeon 34055, Republic of Korea

⁵Department of Astronomy, University of Wisconsin-Madison, 475 N Charter St, Madison, WI 53703, USA

⁵Department of Physics and Astronomy and MQ Research Centre in Astronomy, Astrophysics, and Astrophotonics, Macquarie University, NSW 2109, Australia

⁵Australia Telescope National Facility, CSIRO Space and Astronomy, PO Box 76, Epping NSW 1710, Australia

¹³School of Physical Sciences and Nanotechnology, Yachay Tech University, Hacienda San José S/N, 100119, Urcuquí, Ecuador

⁵International Centre for Radio Astronomy Research (ICRAR), Curtin University, Bentley, WA 6102, Australia

⁵CSIRO Space and Astronomy, 26 Dick Perry Avenue, Kensington, WA 6151, Australia

⁵Department of Physics and Astronomy, University of Calgary, Calgary, AB, Canada T2N 1N4

⁵Max-Planck-Institut für Radioastronomie, Auf dem Hügel 69, 53121 Bonn, Germany

Accepted XXX. Received YYY; in original form ZZZ

ABSTRACT

We present a synergistic analysis of interstellar hydrogen (H_I) and potassium (K_I) absorption from the radio and optical surveys, GASKAP and GALAH, to study the physical and kinematic properties of the cold interstellar medium (ISM) towards the Magellanic Cloud foreground. By comparing GASKAP H_I absorption with interstellar K_I absorption detected in GALAH spectra of nearby stars, we reveal a strong kinematic correlation between these two tracers of the cold neutral ISM. The velocity offsets between matched H_I and K_I absorption components are small, ranging from -5 to $+4$ km s $^{-1}$, with a mean (median) offset of -0.7 (-0.6) km s $^{-1}$. The high degree of kinematic consistency suggests a close spatial association between K_I and cold H_I gas. Correlation analyses reveal a moderate highly statistically significant positive relationship between H_I and K_I line-of-sight properties, such as K_I column density with H_I column density or H_I brightness temperature. We observe a \sim 65% overlap in the detection of both species towards 302 (out of 462) GASKAP H_I absorption lines of sight, and estimate a K_I/H_I abundance ratio of \sim 4.2 \times 10 $^{-10}$, in excellent agreement with previous findings. Our work opens up an exciting avenue of Galactic research that uses large-scale surveys in the radio and optical wavelengths to probe the neutral interstellar medium through its diverse tracers.

Key words: Interstellar line absorption – Interstellar medium – Neutral hydrogen clouds

1 INTRODUCTION

Understanding the structure, composition, and dynamics of the neutral interstellar medium (ISM) is central to unraveling the processes that govern galaxy evolution and star formation (e.g. Draine 2011; Kennicutt & Evans 2012). The neutral ISM is predominantly composed of atomic hydrogen (H_I) and various trace elements, including metals such as potassium (K_I), which together offer complementary insights into its multiphase nature. H_I gas, observable via its 21-cm hyperfine transition, is the primary tracer of neutral atomic material, while neutral potassium, detected through optical absorption lines near 7699 Å, selectively probes the denser and colder regions of the

ISM (Trapero et al. 1995; Welty & Hobbs 2001). Together, these tracers provide a more complete picture of the physical conditions, chemical enrichment, and small-scale structure of the neutral gas.

The neutral atomic hydrogen in the ISM exists in two main thermally stable forms: the warm neutral medium (WNM) with temperature \sim 8000 K and density \sim 0.5 cm $^{-3}$, and the cold neutral medium (CNM) with temperature \sim 100 K and density \sim 10 cm $^{-3}$, for typical Solar metallicity (Field et al. 1969; McKee & Ostriker 1977; Wolfire et al. 2003). While H_I emission generally traces the bulk of the atomic gas across a wide range of temperatures and densities, H_I absorption preferentially traces the CNM at lower temperatures and higher densities (Heiles & Troland 2003; Lee et al. 2015; Murray et al. 2018; Kalberla & Haud 2018; Marchal et al. 2019; Nguyen et al. 2019; McClure-Griffiths et al. 2023; Nguyen et al. 2024).

* E-mail: vanhiep.nguyen@anu.edu.au

Neutral potassium K I provides an additional probe of cold neutral medium. With a low ionization potential (4.34 eV, Corliss & Sugar 1979), K I atoms are more readily photoionized than sodium (Na i) or calcium (Ca ii), resulting in a lower abundance – typically by a factor of ~ 15 compared to Na i and Ca ii (Welty & Hobbs 2001). Consequently, significantly higher total hydrogen column densities N_{H} are required for K I to be detectable, limiting its presence to dense, well-shielded regions where the CNM typically resides (Hobbs 1974a; Welty & Hobbs 2001). This sensitivity to high column density and shielding makes K I an effective tracer of the cold, dense components of the neutral ISM. High-resolution observations of the K I 7699 Å resonance line are particularly useful for resolving interstellar component structures in cases where the more abundant Na i lines become saturated. For instance, interstellar K I absorption has been used to investigate cool H I gas within the local ISM (Trapero et al. 1995), and to explore small-scale spatial structure in high column density environments (Lauroesch & Meyer 1999).

Recent large-scale surveys have revolutionized our ability to study ISM components in detail. In this work, we examine the Galactic ISM from the synergy between two major Galactic surveys: GASKAP (Galactic Australian Square Kilometre Array Pathfinder; Dickey et al. 2013; Pingel et al. 2022) and GALAH (Galactic Archaeology with HERMES; De Silva et al. 2015; Buder et al. 2024). The GASKAP-H I survey provides unprecedented sensitivity and angular resolution ($30''$) in mapping both H I emission and absorption in the direction to the Magellanic System (including Large and Small Magellanic Clouds, Magellanic Bridge, Leading Arms, and Stream as well as their Milky Way foreground). The GALAH spectroscopic survey, meanwhile, offers extensive measurements of interstellar K I absorption features toward a large sample of background stars. The combination of these data sets presents a unique opportunity to study the spatial and kinematic relations between total H I , cold H I (CNM traced by H I absorption) and the dense neutral ISM traced by interstellar K I absorption. Namely, we will investigate (i) the kinematic relationship between H I and K I absorption, and (ii) the abundance of neutral potassium relative to neutral hydrogen.

We focus on the H I clouds at high Galactic latitudes in the Milky Way foreground towards the Magellanic Clouds (MCs) ($b \sim -45^\circ$ to -25°). This region is characterized by distinct filamentary structures, composed of gas and dust, as illustrated in Figure 1. These filamentary structures are likely to reside close to the surface of the Local Bubble, a low-density gas-filled region formed by stellar feedback (Berkhuijsen et al. 1971; Cox & Reynolds 1987; McKee 1998; Zucker et al. 2022), at distances ~ 200 to 300 pc from the Sun (O’Neill et al. 2024; Erceg et al. 2024). In this MC foreground, GASKAP-H I ’s large field of view (5×5 square degrees) facilitates simultaneous measurements of emission and absorption towards 2,714 background continuum sources across a 250 square degree area.

In this work, we utilize H I properties derived from GASKAP-H I absorption measurements with the Pilot Phase II Magellanic Cloud H I foreground observations (Pingel et al. 2022; Nguyen et al. 2024) and K I properties obtained from GALAH Data Release 4 (Buder et al. 2024). Section 2 outlines the observational data sets from GASKAP and GALAH surveys towards the Cirrus region in the Magellanic Cloud foreground. We then examine the kinematic relationship between interstellar K I and H I absorption in Section 3. In Section 4, we discuss H I and K I integrated properties and the K I abundances in the local ISM. Finally, Section 5 summarizes our findings.

2 OBSERVATIONAL DATA

2.1 GASKAP-H I absorption and emission in radio spectra

We utilise H I emission and absorption data from the GASKAP local H I survey (Nguyen et al. 2024). This survey covered an area of ~ 250 square degrees in the direction of Magellanic Clouds, spanning a Galactic latitude range of $b = (-45^\circ, -25^\circ)$ and a Galactic longitude range of $l = (270^\circ, 305^\circ)$. The GASKAP-H I absorption pipeline developed by Dempsey et al. (2022) was employed to extract H I absorption spectra for 2,714 sources. To enhance signal-to-noise sensitivity while still resolving cold H I gas structures, the GASKAP absorption data, initially acquired with a native spectral resolution of 0.244 km s^{-1} were smoothed to a spectral resolution of 0.977 km s^{-1} . Along each H I absorption line of sight, 20 co-located H I emission spectra were also extracted for further Gaussian decomposition analysis. Local H I absorption features were detected at the 3σ threshold towards 462 continuum background sources, resulting in a 17% absorption detection rate, or approximately two detections per square degree. A Gaussian decomposition was then performed on the paired emission-absorption spectra to derive key H I physical properties. For each line of sight, we determine peak optical depths (τ_{peak}), central velocities (v_0), velocity dispersions (Δv_{FWHM}) of individual absorbing gas components, spin temperatures (T_s) of the gas, total H I column densities (N_{HI}), CNM column densities ($N_{\text{HI,CNM}}$), WNM column densities ($N_{\text{HI,WNM}}$), and CNM fractions (f_{CNM}).

The emission survey data were calibrated and reduced using the WSCLEAN software package (Offringa & Smirnov 2017; Van der Tol et al. 2018), which applies standard techniques (such as flagging, calibration, and imaging) with a configuration optimized for wide-field emission (Hotan et al. 2021). In GASKAP spectral line survey, H I radio frequencies at 21 cm (1.42 GHz) are calibrated with extremely high precision using well-established radio frequency standards, such as internal local oscillators or GPS-disciplined ultra-stable quartz/rubidium oscillators, typically achieving Doppler velocity accuracies at the meter-per-second level. We focus on the foreground H I gas in the Milky Way within the velocity range from -50 to $+50 \text{ km s}^{-1}$, where we can detect emission/absorption features above the 3σ threshold, and exclude the velocity range associated with H I emission from the Magellanic Clouds. Overall, the GASKAP-H I survey provides high-resolution observations of H I gas with a synthesized beam $\theta_b = 30$ arcsec towards the MC foreground. Assuming a distance of 220 pc (see Appendix A) to the local gas, the GASKAP beam corresponds to a linear size of ~ 0.03 pc, allowing for a detailed study of the gas physical properties and their relationship with other interstellar components, such as neutral K I and dust.

We show in Figure 1 the positions of 302 matching lines of sight with both H I and interstellar K I absorption detections, overlaid on the GASKAP-H I peak brightness temperature map in Galactic coordinates. An interactive 3D view is available at github.io/gaga. Table 1 summarizes their basic information, including Galactic longitudes/latitudes (l, b), corresponding stars’ Galactic longitudes/latitudes (l^*, b^*), distance to star (D^*), H I and K I column densities ($N_{\text{HI}}, N_{\text{KI}}$), CNM central velocities (V_{CNM}), the corresponding matched K I absorption velocities (V_{KI}), and H I -K I velocity offsets ($\Delta V_{\text{HI-KI}}$) for a sample of 50 lines of sight. A full table containing information for 302 matching H I -K I lines of sight is available in the online version of this publication. All interstellar emission and absorption spectra, along with their kinematic properties, H I and K I

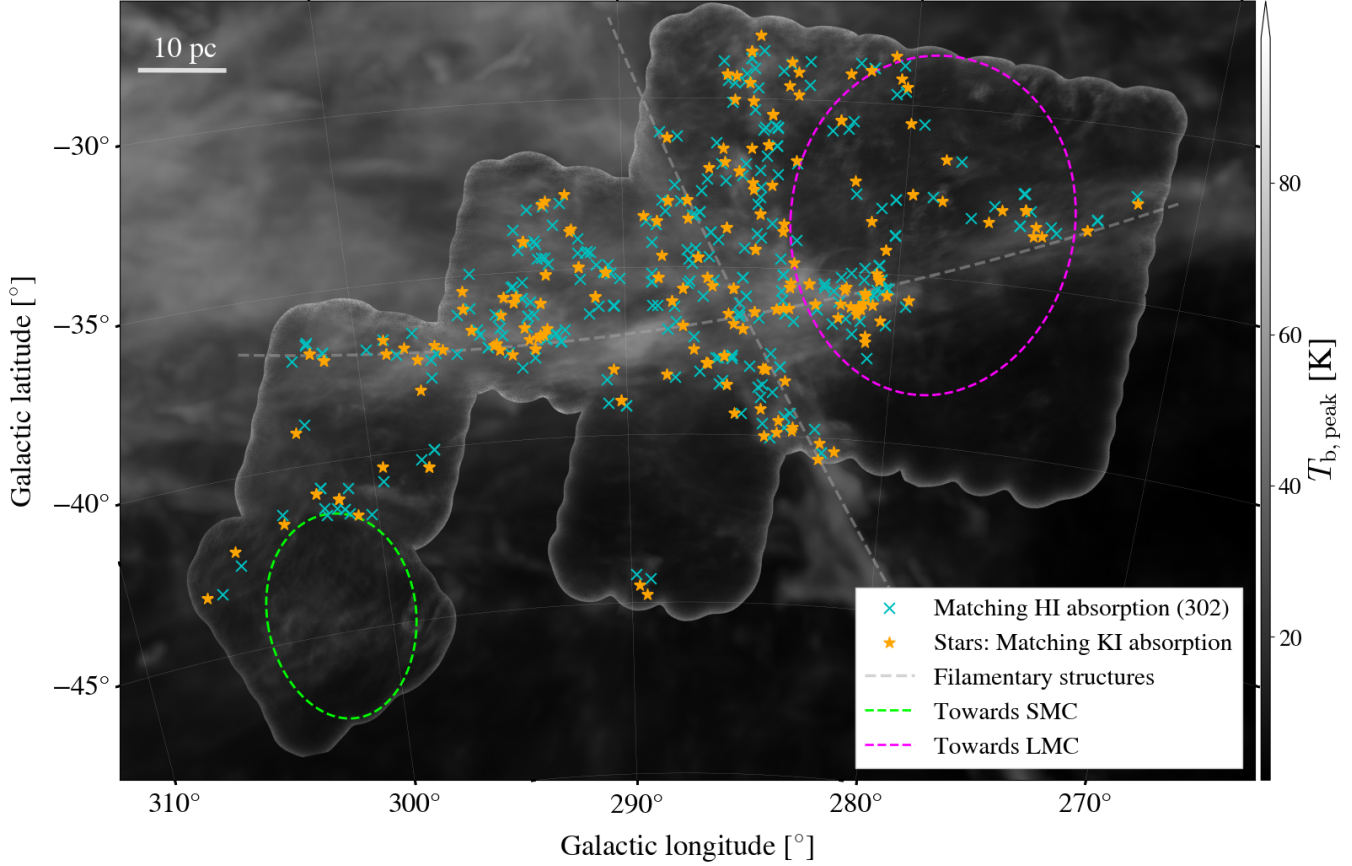


Figure 1. Locations of 302 background radio continuum sources ($S_{1.4 \text{ GHz}} \geq 15 \text{ mJy}$ at 1.4 GHz) in the GASKAP-H_I Pilot II survey with common H_I and K_I absorption detections at the 3σ threshold (crosses), overlaid on the GASKAP peak brightness temperature map ($T_{\text{b},\text{peak}}$, with an angular resolution of $30''$). The gray outer boundary shows the GASKAP-H_I 250-square-degree observing footprint (11 sources per square degree), the GASS peak brightness is shown in the background outside this footprint. The GALAH directions to nearby background stars with matching interstellar K_I detections are shown in star markers. Two local H_I filaments are depicted as gray dashed curves (Reticulum in the vertical direction and Hydrus in the horizontal direction). An interactive 3D view is available at github.io/gaga.

column densities, their associated uncertainties, and the data analysis notebooks are publicly available¹.

2.2 GALAH DR4: Interstellar K_I absorption in optical spectra

The Galactic Archaeology with HERMES (GALAH) Survey Data Release 4 (Buder et al. 2024) provides measurements of high-resolution optical stellar spectra from the High Efficiency and Resolution Multi-Element Spectrograph (HERMES) via the 2dF facility at the 3.9-m Anglo-Australian Telescope (Lewis et al. 2002; Miszalski et al. 2006; Barden et al. 2010; Brzeski et al. 2011; Heijmans et al. 2012; Farrell et al. 2014; Sheinis et al. 2015). HERMES operates with a nominal resolving power of $R = 28,000$ and covers four bands of the optical wavelength range (471–490, 565–587, 648–674, and 759–789 nm). The spectral coverage includes several key ISM absorption features: the atomic K_I absorption line at 7698.9643 Å as well as diffuse interstellar band (DIB) features at 5780.59 Å, 5797.19 Å, and 6613.66 Å (Vogrinčič et al. 2023). The wavelength calibration is performed by fitting a polynomial function

to the identified peak positions of ThXe emission lines from arc calibration frames (Kos et al. 2017). For the fourth band that includes the K_I line, up to 31 peaks can be detected with typical root mean square values of the wavelength solution around 0.027 Å. At the K_I wavelength of 7699 Å, the spectral resolution corresponds to 0.27 Å (or $\sim 10.7 \text{ km s}^{-1}$ in velocity space). The observations are over-sampled on the CCD with a spacing of only 0.0736 Å (equivalent to 2.87 km s⁻¹). The wavelength calibration of optical spectra – without the use of more sophisticated methods like laser frequency combs – is typically much less precise than those of radio observations.

The analysis pipeline of GALAH DR4 fits synthetic stellar spectra, interpolated via neural networks, to the whole wavelength range in order to extract stellar parameters and elemental abundances of up to 32 elements for 917,588 stars, while iteratively shifting the observed spectrum with a global stellar radial velocity.

In modeling stellar spectra, the line spread function (accounting for instrumental and grating effects) and the rotational velocity of a star (which determines stellar rotational broadening) are taken into account. For slow rotators – particularly giant stars, which generally exhibit low rotational velocities – the intrinsic stellar K_I absorption line remains narrow. As a result, it can closely resemble interstellar K_I absorption. For cases where the stellar and ISM line-of-sight

¹ <https://github.com/GASKAP/MW-interstellar-absorption>

Table 1. Basic information of 286 lines of sight with H_I and K_I detections (full table for the sources is available in the online version). For each GASKAP source, we list its Galactic longitudes/latitudes (l, b) as well as the nearby stellar Galactic longitudes/latitudes (l^*, b^*), the star's distance to the Sun (D^*), H_I and K_I column densities ($N_{\text{HI}}, N_{\text{KI}}$), CNM central velocities (V_{CNM}), the corresponding matched K_I absorption velocities (V_{KI}), and H_I-K_I velocity offsets ($\Delta V_{\text{HI-KI}}$).

Source	l ($^{\circ}$)	b ($^{\circ}$)	l^* ($^{\circ}$)	b^* ($^{\circ}$)	D^* (pc)	N_{HI} (10^{20} cm^{-2})	N_{KI} (10^{10} cm^{-2})	V_{CNM} (km s^{-1})	V_{KI} (km s^{-1})	$\Delta V_{\text{HI-KI}}$ (km s^{-1})
J001424-733911	306.49	-43.22	307.10	-43.22	673.5	2.7	25.4	-2.05	-6.15	4.10
J002223-742825	305.56	-42.51	305.70	-42.09	1327.2	2.9	18.9	1.23	3.71	-2.48
J004222-754838	303.67	-41.30	303.68	-41.59	669.0	4.4	33.4	9.95	9.39	0.56
J010120-781900	302.29	-38.80	302.65	-39.00	1055.8	5.1	21.6	5.31	4.06	1.25
J011552-761226	301.01	-40.83	301.43	-41.11	931.6	4.2	20.6	7.33	8.51	-1.18
J012257-751507	300.25	-41.71	300.80	-41.67	989.8	4.3	43.6	7.75	5.74	2.01
J012317-801244	301.25	-36.81	301.22	-37.03	501.9	5.5	21.8	2.73	2.45	0.28
J013252-760405	299.65	-40.80	299.59	-40.37	1432.8	3.6	24.0	1.28	-1.98	3.26
J015425-761348	298.07	-40.30	297.83	-40.55	909.1	4.3	24.3	6.82	6.91	-0.09
J020448-795503	298.99	-36.64	299.00	-36.66	2603.3	5.8	31.7	5.23	5.12	0.11
J020803-792116	298.57	-37.12	298.94	-37.07	2277.1	6.0	16.9	4.00	4.20	-0.20
J021929-781445	297.38	-37.92	297.81	-38.25	2405.8	6.1	17.4	-1.74	-2.87	1.13
J022338-794014	297.92	-36.54	298.26	-36.94	704.9	6.3	38.1	1.52	4.70	-3.18
J022934-784745	297.12	-37.20	297.15	-36.98	879.5	7.0	17.2	2.16	2.84	-0.68
J023934-782554	296.35	-37.28	296.85	-37.13	633.9	7.0	17.9	4.07	3.92	0.15
J024508-695753	289.80	-44.15	289.67	-44.48	813.3	3.8	18.7	8.58	12.86	-4.28
J024800-693600	289.21	-44.29	289.35	-44.77	647.6	3.3	34.0	9.35	11.46	-2.11
J025415-791927	296.21	-36.15	295.98	-35.98	909.4	6.2	32.4	2.24	2.78	-0.54
J025617-780035	295.17	-37.17	294.74	-37.28	563.0	7.0	39.8	1.85	2.00	-0.15
J025618-780044	295.17	-37.17	294.74	-37.28	563.0	7.0	39.8	1.98	2.00	-0.02
J025721-782714	295.43	-36.77	295.74	-36.63	904.6	7.3	23.3	2.65	3.46	-0.81
J025803-783711	295.52	-36.62	295.74	-36.63	904.6	6.5	23.3	1.97	3.46	-1.49
J030316-765256	293.94	-37.85	294.28	-37.45	670.7	5.8	17.4	1.85	1.36	0.49
J030320-791455	295.73	-35.96	295.98	-35.98	909.4	6.7	32.4	1.93	2.78	-0.85
J030330-772932	294.39	-37.36	294.74	-37.28	563.0	7.4	39.8	-0.05	2.00	-2.05
J030705-775917	294.59	-36.85	294.92	-37.12	872.9	9.1	24.8	3.12	3.37	-0.25
J030842-781241	294.68	-36.62	294.85	-37.10	1666.2	7.0	19.7	1.88	4.02	-2.14
J031155-765150	293.44	-37.55	293.43	-37.31	1540.7	6.2	27.7	3.92	3.65	0.27
J031235-782909	294.71	-36.29	294.62	-36.25	583.5	6.0	29.9	1.71	4.42	-2.71
J032019-773939	293.66	-36.65	293.61	-37.03	2788.8	7.0	30.6	2.57	4.75	-2.18
J032113-742002	290.73	-39.04	290.24	-38.97	696.5	5.7	51.0	-4.03	0.64	-4.67
J032253-770007	292.97	-37.04	293.43	-37.31	1540.7	7.9	27.7	3.56	3.65	-0.09
J032255-770011	292.97	-37.03	293.43	-37.31	1540.7	8.0	27.7	3.45	3.65	-0.20
J032259-770023	292.97	-37.03	293.30	-36.98	997.8	7.7	45.5	5.77	5.98	-0.21
J032301-770029	292.97	-37.03	293.43	-37.31	1540.7	8.0	27.7	2.58	3.65	-1.07
J032456-775225	293.62	-36.33	293.77	-36.66	1021.6	6.7	25.0	2.38	4.59	-2.21
J032501-775146	293.60	-36.33	293.77	-36.66	1021.6	6.6	25.0	2.32	4.59	-2.27
J032548-735326	290.04	-39.13	290.24	-38.97	696.5	5.6	51.0	2.52	0.64	1.88
J032550-735329	290.04	-39.13	290.24	-38.97	696.5	5.5	51.0	2.42	0.64	1.78
J032753-774732	293.41	-36.28	293.13	-35.97	687.7	8.1	30.0	2.44	3.81	-1.37
J032816-765522	292.63	-36.88	293.19	-36.93	2460.9	9.3	42.4	2.89	4.82	-1.93
J032819-765520	292.63	-36.88	293.19	-36.93	2460.9	9.0	42.4	2.93	4.82	-1.89
J032822-765517	292.62	-36.88	293.19	-36.93	2460.9	9.1	42.4	2.90	4.82	-1.92
J032834-745053	290.75	-38.33	290.48	-38.03	704.1	9.9	17.1	4.78	4.93	-0.15
J033027-782212	293.79	-35.77	294.10	-35.90	532.8	7.3	21.8	3.01	4.87	-1.86
J033030-782200	293.78	-35.77	294.10	-35.90	532.8	7.4	21.8	2.94	4.87	-1.93
J033037-784908	294.17	-35.44	294.47	-35.71	800.0	6.1	23.2	3.57	2.69	0.88
J033145-784741	294.10	-35.42	294.10	-35.90	532.8	5.7	21.8	4.31	4.87	-0.56
J033211-780653	293.49	-35.89	293.13	-35.97	687.7	7.1	30.0	2.44	3.81	-1.37
J033749-784013	293.74	-35.30	294.00	-35.72	578.9	5.7	48.0	4.73	6.44	-1.71

velocities overlap, the fitting can become degenerate and lead to overestimated stellar K_I abundances while no ISM K_I can be detected in the residuals.

The exciting new aspect of the GALAH DR4 analysis that enables the work presented here, is the separation of stellar and interstellar absorption features in a post-processing step. Buder et al. (2024) achieved this by fitting Gaussian profiles to the residuals of observed and synthetic spectra at particular regions of the spectrum, including ISM absorption components. The fit provides not only the central wavelength to recover the line-of-sight velocity, but also the amplitude and line width (Full Width at Half Maximum, FWHM) which can be converted into an equivalent width. For further details see Buder et al. (2024). We estimate the noise level in the K_I absorption spectra as the standard deviation (σ_{KI}) of off-line wavelength regions. We select stars with (1) residual flux amplitudes ($F_{\text{KI, resid}}$) exceeding $3\sigma_{\text{KI}}$ (three times the noise level); (2) ages older than 1 Gyr to exclude (circum-)stellar contributions to interstellar K_I con-

tent from very young stars; and (3) stellar distances $D_{\star} > 500$ pc, corresponding to the approximate outer distance bound of the Local Bubble shell (e.g., O'Neill et al. 2024; Leike et al. 2020). These selection criteria result in a sample of 9,819 stars across the region of interest towards the Magellanic Cloud foreground (see Figure 5 below).

As recommended by Buder et al. (2024), we apply the velocity correction of the fit via the stellar radial velocity to recover the true line-of-sight velocity of the interstellar K_I line rather than the incorrectly listed one. This correction allows us to now match the K_I absorption components with the H_I absorption Gaussian components identified in the GASKAP-H_I survey.

3 KINEMATIC RELATIONSHIP BETWEEN INTERSTELLAR K_I AND H_I ABSORPTION

We examine the kinematic relationship between CNM and interstellar K_I absorption features by combining data from the GASKAP-H_I survey (462 H_I absorption-detected lines of sight) and the GALAH DR4 catalogue (9,819 selected stars, as detailed in Section 2.2). To establish reliable matches and enable meaningful comparisons between these two datasets, we consider both spatial (on-sky) and spectral properties.

For spatial matching in the plane of sky, we adopted a search radius of 0.5 degrees around each GASKAP-H_I absorption sightline to identify candidate stars from the GALAH DR4 survey. Assuming a typical distance of 220 pc (see Appendix A) to the absorbing gas, this angular radius corresponds to a linear scale of ~ 2 pc. This value represents a balance between maintaining physical association with the absorbing gas and retaining a statistically significant number of matched stars. Along the GASKAP-H_I sightlines, the number of nearby GALAH stars varies between 15 and 80.

To enable direct spectral comparison, we converted the GALAH stellar spectra from wavelength to Doppler velocity in the kinematic Local Standard of Rest (LSRK) frame, using the Solar peculiar motion ($(U_{\odot}, V_{\odot}, W_{\odot}) = (11.10, 12.24, 7.25)$ km s⁻¹ (Schönrich et al. 2010), where U_{\odot} is directed towards the Galactic center, V_{\odot} is in the direction of Galactic rotation, and W_{\odot} points towards the north Galactic pole. This transformation ensures consistency with the velocity frame adopted in the GASKAP-H_I observations. Among the matched stars, we select a subset based on the following further criteria: (1) smallest angular separations from the GASKAP-H_I line of sight; (2) velocity offset between K_I and H_I absorption components $\Delta V_{\text{CNM-KI}} < 5$ km s⁻¹ (about half the GALAH K_I resolution), using Gaussian-fitted central velocities; (3) high K_I signal-to-noise: K_I equivalent width $EW_{\text{KI}} > 0.035$ Å and residual flux amplitude $F_{\text{KI,resid}} > 3\sigma_{\text{KI}}$; (4) clear separation between stellar and interstellar K_I absorption features $\Delta V_{\text{KI}}^{\star} > 10$ km s⁻¹ (GALAH’s K_I spectral resolution). Applying these criteria resulted in 302 out of 462 GASKAP-H_I lines of sight with confident detections of both H_I and interstellar K_I absorption features, yielding a matching interstellar absorption detection rate of $\sim 65\%$.

The kinematic correlation between the central velocities of the K_I and H_I absorption components is shown in Figure 2 top panel, with their velocity offsets $\Delta V_{\text{CNM-KI}}$ (here $V_{0,\text{CNM}} - V_{0,\text{KI}}$) displayed in the lower panel. The strong correlation, with Pearson and Spearman coefficients both at 0.9 and p -values = 0 implies a close kinematic association between interstellar K_I and CNM, indicating their co-movement (and possibly even co-existence) in the Galactic ISM.

The uncertainties in CNM velocities, derived from Gaussian decomposition in GASKAP-H_I are typically lower than 0.25 km s⁻¹; but for simplicity, here we assume a uniform maximum uncertainty of 0.5 km s⁻¹ (half of H_I channel width). For the K_I velocities, we adopt the GALAH K_I spectral resolution of 10.7 km s⁻¹ as a reference, leading to an estimated uncertainty of ~ 5 km s⁻¹ per individual measurement (i.e., half the resolution). Since multiple nearby stars are used per GASKAP-H_I line of sight, and assuming that each measurement is independent, we reduce the uncertainty in the mean K_I velocity by calculating the standard error $\sigma_{V,\text{KI}} = 5/\sqrt{N^{\star}}$ km s⁻¹, where N^{\star} is the number of contributing stars. The 68% confidence bounds in Figure 2 are estimated using bootstrap resampling of only K_I velocity uncertainties (which are an order of magnitude larger than those for the CNM central velocity) and reflect the maximum uncertainty interval.

The H_I-K_I velocity offsets range from -5 km s⁻¹ to $+4$ km s⁻¹,

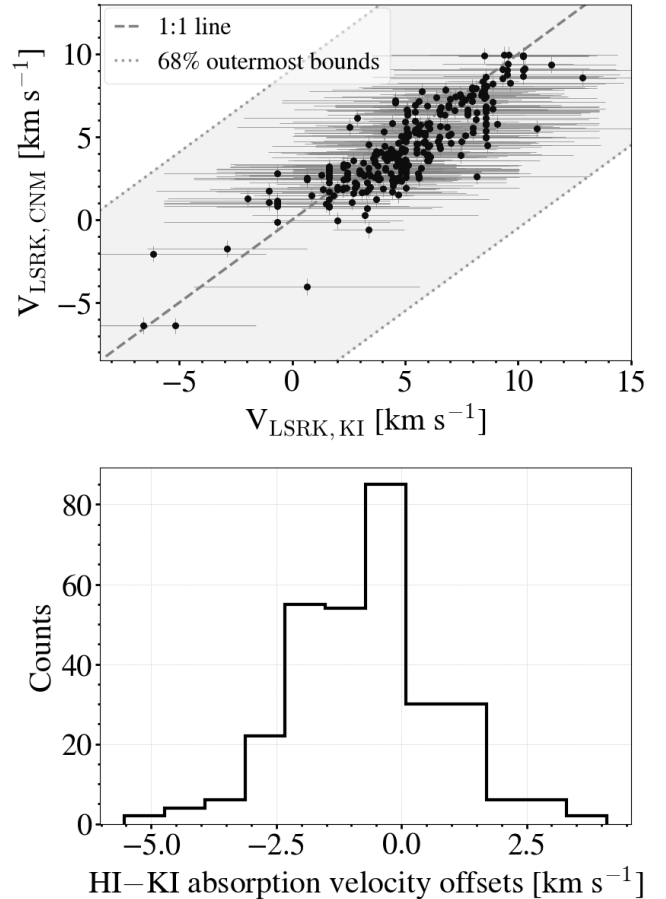


Figure 2. Top: Comparison of CNM and K_I absorption velocities. See Section 3 for details on the estimation of velocity uncertainties and the 68% confidence intervals. Bottom: Histogram of velocity offsets between CNM and K_I absorption features ($V_{\text{CNM}} - V_{\text{KI}}$).

with a mean of -0.7 km s⁻¹, a median of -0.6 km s⁻¹, and a standard deviation of 1.5 km s⁻¹. For comparison, Piecka et al. (2024) recently reported excellent agreement between the interstellar radial velocities of K_I and Ca II for their 47 targets probing an outflow from the Scorpius–Centaurus OB association. They also noted the presence of small systematic differences between calcium and hydrogen velocities, typically less than 5 km s⁻¹ (in the range of 2–3 km s⁻¹). In our case, given the relatively large uncertainties in the K_I central velocities due to its original spectral resolution ~ 10.7 km s⁻¹, we believe that the slight scatter in the velocity offsets seen in Figure 2 does not reflect real physical differences.

Since the K_I lines of sight are selected to be close to those of H_I absorption, and if we interpret velocity as a proxy for spatial location (e.g., CNM components at different velocities correspond to different distances), then our results implies that K_I is likely located within or near CNM environments. This interpretation is consistent with previous analyses that reveal strong kinematic associations between CNM and molecular gas, such as CO (e.g., Park et al. 2023) and OH (e.g., Hafner et al. 2023), in high-density, low-temperature regimes.

Hi Jo! any other references for OH and CNM here?

We note that whenever H_I absorption is undetected, K_I absorption features also tend to be absent above the 3σ threshold. Additionally, ISM K_I absorption features are consistently narrower than H_I emission lines, but generally broader than H_I absorption features (see

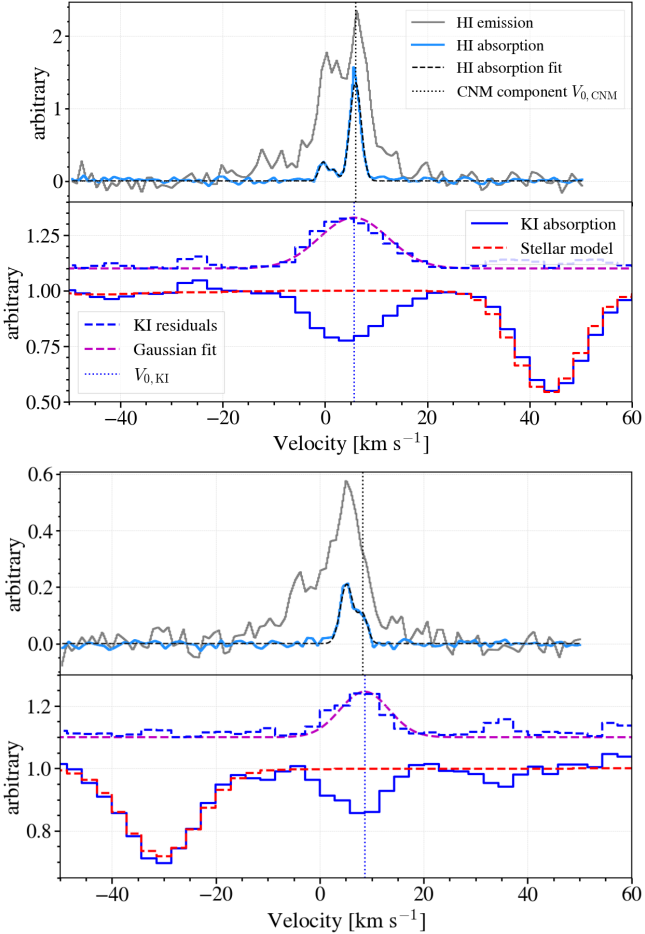


Figure 3. HI/KI sample spectra towards the Magellanic Cloud foreground. Top panels: HI emission (grey), absorption (light blue), and a Gaussian fit to the HI absorption profile (black dashed line). The central velocity of a CNM component is indicated by the vertical dotted line. Bottom panels: GALAH stellar spectrum (blue solid line), synthetic stellar spectrum (red solid line), residual KI absorption (blue dashed line), and a Gaussian fit to the KI residual (magenta dashed line). The vertical dotted line indicates the central velocity of the KI absorption component, which aligns with the CNM central velocity. The y-axes in all panels represent arbitrary units and are not scaled. More samples are available at [GASKAP Github repository](#).

Figure 3 for examples). However, we believe that the apparent widths of the KI absorption features are influenced by the relatively low spectral resolution (10.7 km s^{-1}). Higher-resolution stellar spectroscopy observations are required to confirm this interpretation.

4 INTEGRATED PROPERTIES: KI VS HI

In this Section we explore a possible quantitative relationship between KI and HI neutral species as well as the KI/HI abundance. We define the relative abundance of neutral potassium KI with respect to neutral hydrogen HI as the ratio of their respective integrated column densities, $N_{\text{KI}}/N_{\text{HI}}$. HI column density is obtained from the GASKAP absorption survey, and therefore is corrected for the opacity effect. The KI column density is derived from the KI equivalent width (listed in GALAH DR4 as `ew_k_is`), which is measured by Gaussian fits to the residuals between the GALAH observed spectra and the corresponding stellar models (as depicted by the blue dashed

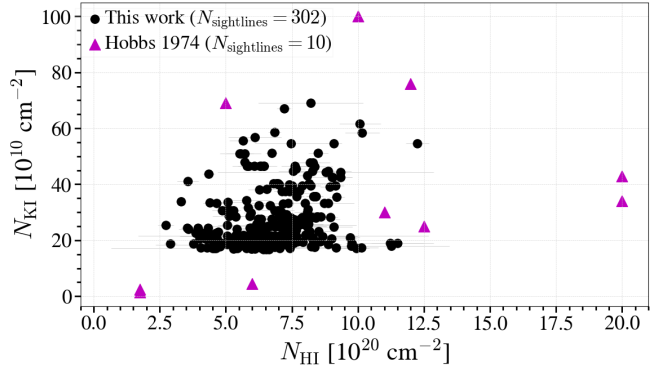


Figure 4. Opacity-corrected HI vs KI column densities. Circles represent our sample for 302 lines of sight, triangles indicate Hobbs (1974a)'s sample of ten lines of sight.

line in Figure 3). Subsequently, assuming the interstellar KI line to be optically thin, we can employ the linear regime of the curve of growth, which establishes a direct proportionality between the KI column density N_{KI} and its equivalent width EW_{KI} :

$$N_{\text{KI}} \frac{\pi e^2 f \lambda^2}{m_e c^2} = \int (-\ln r_\nu) d\nu \approx EW_{\text{KI}}, \quad (1)$$

with KI wavelength λ at 7698.9643\AA , residual intensity r_ν for a frequency ν , as well as electron charge e , electron mass m_e , speed of light c , and oscillator strength f (Hobbs 1974b). For the KI the resonance transition between the first excited electronic state to the ground electronic state ($3p^6 4p^2 P_{3/2} \rightarrow 3p^6 4s^2 S_{1/2}$), we adopted a logarithm of the oscillator strength $\log g_f = -0.178$ from Trubko et al. (2017). Given the statistical weight of the lower level ($g = 2J + 1 = 2$ for the $3p^6 4s^2 S_{1/2}$ state with a total angular momentum $J = 1/2$) and the provided $\log g_f$ value, this corresponds to an oscillator strength f -value = 0.332.

Below, we perform correlation analyses using both the Hobbs (1974a) dataset (a small sample of ten lines of sight with relatively broad Galactic longitude coverage) and our own dataset consisting of 302 matched lines of sight. This comparison allows us to assess the consistency and statistical significance of any potential trends between KI and HI column densities. In addition, we extend our analysis to a larger, complete sample of 9,819 selected stars by comparing GALAH KI column densities with GASKAP HI peak brightness temperatures and column densities under the optically-thin assumption.

4.1 KI-HI relation

We first examine the KI and HI column density values reported by Hobbs (1974a, triangle markers in Figure 4). Hobbs (1974a) determined their opacity-corrected HI column densities from Lyman- α measurements obtained with the Orbiting Astronomical Observatory 2 (OAO-2, Savage & Jenkins 1972). Pearson and Spearman correlation analyses for their ten sightlines yield coefficients of 0.31 (p -value = 0.38) and 0.45 (p -value = 0.20), respectively. While both coefficients show positive trends, their associated p -values are well above the conventional significance threshold of 0.05. Due to their small sample size, we cannot confidently conclude the presence of a statistically significant linear or monotonic relationship between KI and HI based on Hobbs (1974a) data, as the observed trends could readily be attributed to random chance within such a limited dataset.

In contrast, our correlation analyses along 302 matched lines of

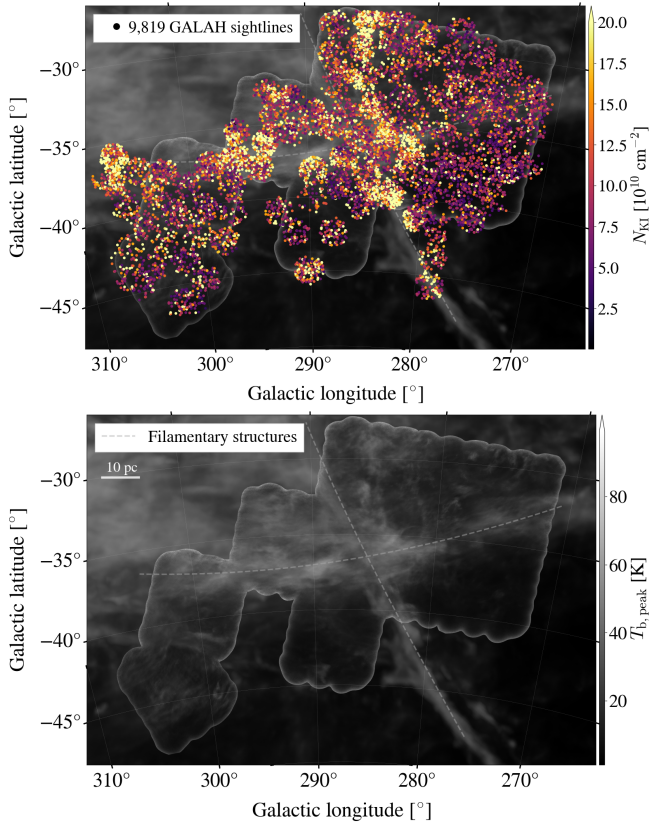


Figure 5. Spatial on-sky distribution of GALAH K_I column density measurements towards 9,819 stars in the Magellanic Cloud foreground, overlaid on the GASKAP H_I peak brightness temperature map $T_{\text{b},\text{peak}}$.

sight reveal a moderate, statistically significant positive relationship between opacity-corrected H_I and K_I column densities (indicated by circle markers in Figure 4). The Pearson correlation coefficient is 0.27, whereas the Spearman coefficient is 0.28. Both correlation tests are highly statistically significant, with small p -values of 2×10^{-6} and 1×10^{-6} , respectively. This strong statistical significance, supported by a substantial sample size of 302 matched sightlines, suggests a modest positive association between H_I and K_I.

We then further examine the H_I-K_I line-of-sight properties for a complete sample of 9,819 selected lines of sight using optically-thin H_I column density N_{HI}^* ; peak brightness temperature $T_{\text{b},\text{peak}}$ from H_I emission data, and K_I column density N_{KI} . An on-sky distribution of K_I column densities towards 9,819 stars, as shown in Figure 5, reveals a distinctive spatial behavior. While the K_I column density distribution broadly follows the morphology of H_I filamentary structures characterized by high column densities ($N_{\text{HI}}^* > 5 \times 10^{20} \text{ cm}^{-2}$) and peak brightness temperature ($T_{\text{b},\text{peak}} > 40 \text{ K}$), it also appears to be distinctly clumpy scattered across the map. Figure 6 compares N_{KI} with both N_{HI}^* and $T_{\text{b},\text{peak}}$; here, circle markers and shaded regions represent median values and 1σ uncertainties in column density and brightness temperature bins.

In these subsequent broader analyses, both Pearson and Spearman correlation analyses indicate statistically significant positive relationships between H_I and K_I properties. For the $N_{\text{HI}}^*-N_{\text{KI}}$ pair, the Pearson correlation coefficient is 0.24 (p -value = 0), while the Spearman rank correlation is slightly higher at 0.34 (p -value = 0). The correlation between N_{KI} and $T_{\text{b},\text{peak}}$ is similarly positive, with a Pear-

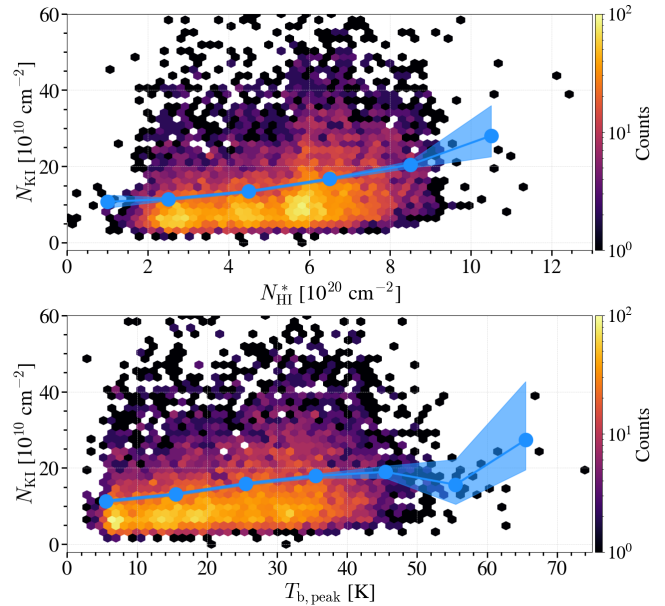


Figure 6. Correlations between H_I and K_I line-of-sight properties towards 9,819 stars in the Magellanic Cloud foreground. Top panel: K_I column density (N_{KI}) versus optically-thin H_I column density (N_{HI}^*). Bottom panel: K_I column density versus H_I peak brightness temperature ($T_{\text{b},\text{peak}}$). For clarity, N_{KI} above $60 \times 10^{10} \text{ cm}^{-2}$ are truncated. Circles and shaded regions denote median values and their 1σ uncertainties per N_{HI}^* and $T_{\text{b},\text{peak}}$ bins, respectively. Color indicates data point density.

son coefficient of 0.23 (p -value = 0), and a Spearman coefficient of 0.31 (p -value = 0). The high statistical significance (indicated by extremely low p -values, effectively zero) across the latter analyses confirms that these positive H_I-K_I correlations are unlikely to be due to random chance. In all comparisons carried out in this Section, the Spearman correlation coefficients are higher than their respective Pearson coefficients. This suggests that while N_{KI} tends to increase as N_{HI} (or $T_{\text{b},\text{peak}}$) increases, their relationships might be better described by a general increasing trend rather than a linear one.

These findings indicate that, across a large sample of sightlines in the Magellanic Cloud foreground, the presence of neutral potassium K_I is generally associated with higher H_I content and stronger H_I emission, albeit with considerable scatter due to local ISM complexity. A low energy threshold to the first excited state means that K_I atoms can be readily ionized by interstellar radiation fields, potentially creating variations in K_I abundance. To quantify this, we apply the Saha collisional ionization equation under assumptions of thermal equilibrium and the absence of external ionizing sources and find that, for a broad range of electron densities ($n_e = 10^{-3} - 1 \text{ cm}^{-3}$), nearly all potassium atoms are ionized at temperatures around 1000 K and change to neutral for temperatures ~ 100 K lower. Consequently, the presence of K_I atoms is likely sensitive to local radiation and thermal conditions (temperature and density), with stellar radiation and high-temperature regions capable of dramatically altering K_I abundance across interstellar environments. Neutral potassium samples relatively denser atomic material than H_I and other atomic lines such as Ca II and Na I (e.g. Welty & Hobbs 2001). Therefore, K_I observations may be dominated by small-scale fluctuations in the density distribution that may not always coincide with H_I distribution on larger scales.

[HN: Regarding Saha equation. Message from Denis: I confirm

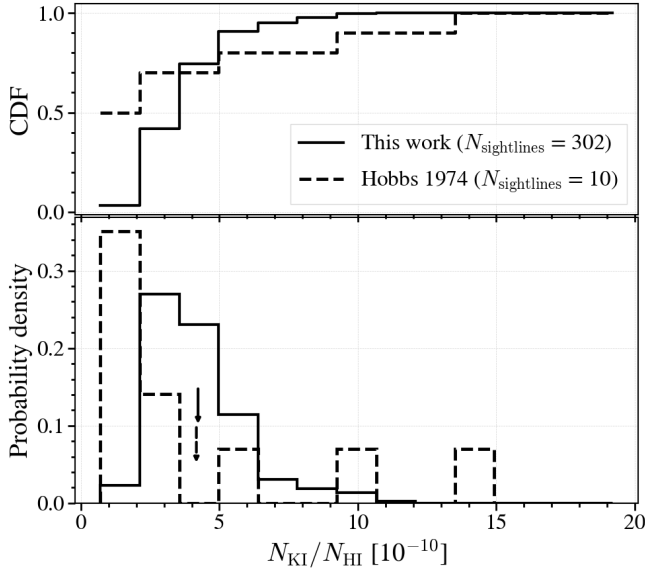


Figure 7. Distributions of KI/HI abundance ratios (lower panel), i.e. KI/HI column density ratios, and their cumulative distribution functions (CDF, upper panel). The solid line represents our current work (302 lines of sight), whereas the dashed line shows data from Hobbs 1974a (ten lines of sight). Arrows indicate the average values for each sample, both at $\sim 4.2 \times 10^{-10}$.

your results: because ne is very low the temperature to ionize H is very low (about 3000K, but I just put in a guess for the partition functions of neutral and ionized H). Similarly for KI is very low, about 600K.]

HN: (Thanks Hilay!) In case of Hydrgen gas: It should be said, by the way, that in reality the WNM has a temperature of about 8000 K. This is an indication that one or more of our assumptions (with the use of Saha equation) is not correct. That assumption is that the radiation field is in thermal equilibrium with the matter. In fact, the ionizing radiation field is provided mainly by UV from hot stars, rather than a constant thermal bath. Thus even though we did not get quite the right answer, (1) we did get within a factor of a few, and (2) the fact that comparison with observations shows we're not quite there tells us that we need to know something extra.

HN: I am checking this using “CLOUDY”

4.2 KI/HI abundance

The distribution of the resulting KI/HI abundance ratios across our sample of 302 matching lines of sight is presented in Figure 7, alongside a comparison with the findings of Hobbs 1974a (ten lines of sight). Our analysis reveals a KI/HI abundance ratio ranging from 1.6×10^{-10} to 11.6×10^{-10} , with a mean (median, standard deviation) of 4.2×10^{-10} (3.8×10^{-10} , 1.7×10^{-10}). For the ten lines of sight examined by Hobbs (1974a, see their Table 1), the reported KI/HI abundance ratios span from 0.7×10^{-10} to 13.8×10^{-10} , with a mean (median, standard deviation) of 4.2×10^{-10} (2.1×10^{-10} , 4.5×10^{-10}). The excellent consistency between the statistical properties of the KI/HI abundance ratios derived from our significantly larger sample and those reported in literature provides strong support for the reliability of our KI abundance estimates and suggests a degree of uniformity in these ratios across different lines of sight probed by the two studies.

To assess whether the two samples originate from the same underlying distribution, we perform a two-sample Kolmogorov-Smirnov (KS) test. The test yields a KS statistic of 0.581 with a p -value of 10^{-3} . Given this statistically significant p -value < 0.05 , there exists a significant difference between the two KI/HI abundance ratio distributions.

5 CONCLUSIONS AND FUTURE WORK

We have conducted a joint multi-wavelength analysis of the local neutral ISM with the use of two large-scale surveys: GASKAP for HI absorption at 21 cm and GALAH optical spectroscopy for KI absorption at 7699 Å. Leveraging the Gaussian decompositions performed by Nguyen et al. (2024) for 462 GASKAP lines of sight with HI absorption detections, together with GALAH measurements of interstellar KI absorption in the spectra of nearby stars by Buder et al. (2024), we investigated the kinematic relationship between CNM and neutral potassium in the Solar neighborhood at large Galactic latitudes Galactic latitudes (-45° , -25°) in the foreground of the Magellanic Clouds. The region of interest encompasses prominent HI filamentary structures, as seen in Figure 1.

Our key findings are as follows:

- (i) Along 462 GASKAP lines of sight with HI absorption detections, we identified 302 ($\sim 65\%$) overlapping lines of sight showing absorption in both HI and KI neutral species.
- (ii) We find a strong kinematic correlation between these two tracers of cold neutral ISM in the Magellanic Cloud foreground. The small velocity offsets observed between corresponding HI and KI absorption features suggest a close physical association, suggesting that KI absorption likely arises within regions of cold hydrogen gas. In addition, a moderate, highly-statistically-significant positive correlation is found when examining HI and KI line-of-sight quantities, such as KI column density compared to HI column density or HI brightness.
- (iii) Our derived KI/HI abundance ratio is in excellent agreement with previous measurements reported by Hobbs (1974a), both at $\sim 4.2 \times 10^{-10}$.
- (iv) Our GASKAP-GALAH synergy highlights the power of combining large-scale radio and optical surveys to gain new insights into the structure and composition of the local neutral ISM.

Building upon strong HI-KI kinematic correlation found in this study, our future work will characterise the physical properties and spatial distribution of the local absorbing species across the sky, using HI absorption detected in all existing Galactic absorption surveys. A key next step will be to estimate distances to the detected HI gas features using the high-resolution GASKAP data in conjunction with detailed 3D dust maps of the Galactic ISM. Furthermore, we will establish a 3D field of H α emission by modelling the transport of H α photons and applying Gaussian inference to the well-constrained distances of nearby Solar neighborhood stars. By correlating the 3D distribution of HI and KI absorption with the derived 3D H α emission field, we will be able to investigate the ionization state of hydrogen gas and explore the interplay between neutral and ionized components of the local ISM on larger scales.

ACKNOWLEDGEMENTS

This scientific work uses data obtained from Inyarrimanna Ilgari Bundara / the Murchison Radio-astronomy Observatory. We acknowledge the Wajarri Yamaji People as the Traditional Owners

and native title holders of the Observatory site. CSIRO's ASKAP radio telescope is part of the Australia Telescope National Facility (<https://ror.org/05qajvd42>). Operation of ASKAP is funded by the Australian Government with support from the National Collaborative Research Infrastructure Strategy. ASKAP uses the resources of the Pawsey Supercomputing Research Centre. Establishment of ASKAP, Inyarrimanna Ilgari Bundara, the CSIRO Murchison Radioastronomy Observatory and the Pawsey Supercomputing Research Centre are initiatives of the Australian Government, with support from the Government of Western Australia and the Science and Industry Endowment Fund.

This research was partially funded by the Australian Government through an Australian Research Council Australian Laureate Fellowship (project number FL210100039) to NMc-G and a Discovery Early Career Researcher Award (DE240100150) to SB. JDS acknowledges funding by the European Research Council via the ERC Synergy Grant “ECOGAL – Understanding our Galactic ecosystem: From the disk of the Milky Way to the formation sites of stars and planets” (project ID 855130). SEC acknowledges support from NSF award AST-2106607 and an Alfred P. Sloan Research Fellowship.

This work made use of the Fourth Data Release of the GALAH Survey (Buder et al. 2024). The GALAH Survey is based on data acquired through the Australian Astronomical Observatory, under programs: A/2013B/13 (The GALAH pilot survey); A/2014A/25, A/2015A/19, A/2017A/18 (The GALAH survey phase 1); A/2018A/18 (Open clusters with HERMES); A/2019A/1 (Hierarchical star formation in Ori OB1); A/2019A/15, A/2020B/23, R/2022B/5, R/2023A/4, R/2023B/5 (The GALAH survey phase 2); A/2015B/19, A/2016A/22, A/2016B/10, A/2017B/16, A/2018B/15 (The HERMES-TESS program); A/2015A/3, A/2015B/1, A/2015B/19, A/2016A/22, A/2016B/12, A/2017A/14, A/2020B/14 (The HERMES K2-follow-up program); R/2022B/02 and A/2023A/09 (Combining asteroseismology and spectroscopy in K2); A/2023A/8 (Resolving the chemical fingerprints of Milky Way mergers); and A/2023B/4 (s-process variations in southern globular clusters). We acknowledge the traditional owners of the Country on which the AAT stands, the Gami-laraay people, and pay our respects to Elders past and present. This paper includes data that has been provided by AAO Data Central (datacentral.org.au).

This work has made use of data from the European Space Agency (ESA) mission Gaia (<https://www.cosmos.esa.int/gaia>), processed by the Gaia Data Processing and Analysis Consortium (DPAC, <https://www.cosmos.esa.int/web/gaia/dpac/consortium>). Funding for the DPAC has been provided by national institutions, in particular the institutions participating in the Gaia Multilateral Agreement.

Software: Astropy (Paszke et al. 2019), Matplotlib (Hunter 2007), NumPy (van der Walt et al. 2011), SciPy (Virtanen et al. 2020), Pandas (McKinney et al. 2010).

DATA AVAILABILITY

This paper includes archived data obtained through the CSIRO ASKAP Science Data Archive, CASDA (<https://research.csiro.au/casda>).

The GASKAP emission and absorption data used in this study, along with the fitted results and their associated uncertainties are derived by Nguyen et al. (2024) and available at [GASKAP Github repository](#).

All data related to the GALAH survey (<https://www.galah-survey.org/>) are publicly available at https://cloud.datacentral.org.au/teamdata/GALAH/public/GALAH_DR4/.

REFERENCES

- Barden S. C., et al., 2010, *SPIE*, 7735, 09
 Berkhuijsen E. M., Haslam C. G. T., Salter C. J., 1971, *A&A*, 14, 252
 Brzeski J., Case S., Gers L., 2011, *SPIE*, 8125, 04
 Buder S., et al., 2024, arXiv e-prints, p. arXiv:2409.19858
 Corliss C., Sugar J., 1979, *Journal of Physical and Chemical Reference Data*, 8, 1109
 Cox D. P., Reynolds R. J., 1987, *ARA&A*, 25, 303
 De Silva G. M., et al., 2015, *MNRAS*, 449, 2604
 Dempsey J., et al., 2022, *PASA*, 39, e034
 Dickey J. M., et al., 2013, *PASA*, 30, e003
 Draine B. T., 2011, Physics of the Interstellar and Intergalactic Medium
 Edenhofer G., Zucker C., Frank P., Saydari A. K., Speagle J. S., Finkbeiner D., Enßlin T. A., 2024, *A&A*, 685, A82
 Erceg A., Jelić V., Haverkorn M., Bracco A., Ceraj L., Turić L., Soler J. D., 2024, *A&A*, 687, A23
 Farrell T. J., Birchall M. N., Heald R. W., Shortridge K., Vuong M. V., Sheinis A. I., 2014, *SPIE*, 9152, 23
 Field G. B., Goldsmith D. W., Habing H. J., 1969, *ApJ*, 155, L149
 Gaia Collaboration et al., 2023, *A&A*, 674, A1
 Górski K. M., Hivon E., Banday A. J., Wandelt B. D., Hansen F. K., Reinecke M., Bartelmann M., 2005, *ApJ*, 622, 759
 HI4PI Collaboration et al., 2016, *A&A*, 594, A116
 Hafner A., et al., 2023, *PASA*, 40, e015
 Heijmans J., et al., 2012, *SPIE*, 8446, 0W
 Heiles C., Troland T. H., 2003, *ApJS*, 145, 329
 Hobbs L. M., 1974a, *ApJ*, 188, L67
 Hobbs L. M., 1974b, *ApJ*, 191, 381
 Hotan A. W., et al., 2021, *PASA*, 38, e009
 Hunter J. D., 2007, *Computing in Science & Engineering*, 9, 90
 Kalberla P. M. W., Haud U., 2018, *A&A*, 619, A58
 Kennicutt R. C., Evans N. J., 2012, *ARA&A*, 50, 531
 Kerp J., Winkel B., Ben Bekhti N., Flöer L., Kalberla P. M. W., 2011, *Astronomische Nachrichten*, 332, 637
 Kos J., et al., 2017, *MNRAS*, 464, 1259
 Lauroesch J. T., Meyer D. M., 1999, *ApJ*, 519, L181
 Lee M.-Y., Stanimirović S., Murray C. E., Heiles C., Miller J., 2015, *ApJ*, 809, 56
 Leike R. H., Glatzle M., Enßlin T. A., 2020, *A&A*, 639, A138
 Lewis I. J., et al., 2002, *MNRAS*, 333, 279
 Marchal A., Miville-Deschénes M.-A., Orieux F., Gac N., Soussen C., Lesot M.-J., d'Allonne A. R., Salomé Q., 2019, *A&A*, 626, A101
 McClure-Griffiths N. M., et al., 2009, *ApJS*, 181, 398
 McClure-Griffiths N. M., Stanimirović S., Rybicky D. R., 2023, *Annual Review of Astronomy and Astrophysics*, 61, null
 McKee C. F., 1998, in Breitschwerdt D., Freyberg M. J., Truemper J., eds., Vol. 506, IAU Colloq. 166: The Local Bubble and Beyond. pp 565–580
 McKee C. F., Ostriker J. P., 1977, *ApJ*, 218, 148
 McKinney W., et al., 2010, in Proceedings of the 9th Python in Science Conference, pp 51–56
 Miszalski B., Shortridge K., Saunders W., Parker Q. A., Croom S. M., 2006, *MNRAS*, 371, 1537
 Murray C. E., Stanimirović S., Goss W. M., Heiles C., Dickey J. M., Babler B., Kim C.-G., 2018, *ApJS*, 238, 14
 Nguyen H., Dawson J. R., Lee M.-Y., Murray C. E., Stanimirović S., Heiles C., Miville-Deschénes M. A., Petzler A., 2019, *ApJ*, 880, 141
 Nguyen H., et al., 2024, *MNRAS*, 534, 3478
 O'Neill T. J., Zucker C., Goodman A. A., Edenhofer G., 2024, arXiv e-prints, p. arXiv:2403.04961
 Offringa A. R., Smirnov O., 2017, *MNRAS*, 471, 301
 Park G., et al., 2023, *ApJ*, 955, 145
 Paszke A., et al., 2019, arXiv e-prints, p. arXiv:1912.01703
 Piecka M., Hutschenreuter S., Alves J., 2024, *A&A*, 689, A84
 Pingel N. M., et al., 2022, *PASA*, 39, e005
 Savage B. D., Jenkins E. B., 1972, *ApJ*, 172, 491
 Schönrich R., Binney J., Dehnen W., 2010, *MNRAS*, 403, 1829
 Sheinis A., et al., 2015, *J. Astron. Telesc. Instrum. Syst.*, 1, 035002

- Soler J. D., et al., 2019, *A&A*, **622**, A166
 Soler J. D., et al., 2025, *A&A*, **695**, A222
 Trapero J., Beckman J. E., Serra-Ricart M., Davies R. D., Watson R. A.,
 Garcia Lopez R. J., 1995, *ApJ*, **445**, 231
 Trubko R., Gregoire M. D., Holmgren W. F., Cronin A. D., 2017, *Phys.
 Rev. A*, **95**, 052507
 Van der Tol S., Veenboer B., Offringa A. R., 2018, *A&A*, **616**, A27
 Virtanen P., et al., 2020, *Nature Methods*, **17**, 261
 Vogrinčič R., et al., 2023, *MNRAS*, **521**, 3727
 Welty D. E., Hobbs L. M., 2001, *ApJS*, **133**, 345
 Winkel B., Kalberla P. M. W., Kerp J., Flöer L., 2010, *ApJS*, **188**, 488
 Wolfire M. G., McKee C. F., Hollenbach D., Tielens A. G. G. M., 2003, *ApJ*,
587, 278
 Zhang X., Green G. M., Rix H.-W., 2023, *MNRAS*, **524**, 1855
 Zucker C., et al., 2022, *Nature*, **601**, 334
 van der Walt S., Colbert S. C., Varoquaux G., 2011, *Computing in Science
 and Engineering*, **13**, 22

APPENDIX A: LINKING HI GAS TO PHYSICAL DISTANCE USING 3D DUST EXTINCTION AND HI4PI

In order to estimate physical distances to the local HI gas, we utilize the recently released 3D map of interstellar dust extinction by Edenhofer et al. (2024) in conjunction with the HI4PI data cube (HI4PI Collaboration et al. 2016).

The 3D dust map provides the distribution of differential extinction between 69 out to 1250 pc from the Sun. This map offers an angular resolution of ~ 13.7 arcmin (HEALPix² resolution parameter $N_{\text{side}} = 256$) and a distance resolution of 2 pc. Built upon Gaia mission data (Gaia Collaboration et al. 2023), the 3D dust reconstruction employs a Gaussian process to model differential dust extinction in spherical coordinates for 54 million nearby stars, assuming a spatially smooth distribution of dust extinction. The differential extinction is given in unitless values, defined by Zhang et al. (2023) (hereafter ZGR23) as $(dA_{\text{ZGR23}}/1 \text{ pc})$. These extinction units can be converted into extinction at a specific wavelength using the publicly available ZGR23 extinction curve³.

For HI emission, we employ the HI4PI data cube, constructed from the Effelsberg-Bonn HI Survey (EBHIS; Winkel et al. 2010; Kerp et al. 2011) and the Galactic All-Sky Survey (GASS; McClure-Griffiths et al. 2009) single-dish observations. The combined set has an angular resolution of 16.2 arcmin and a sensitivity of 43 mK per 1.29 km s^{-1} spectral resolution. This angular resolution is close to the 14 arcmin resolution of the 3D dust map. Assuming HI kinematics as a proxy for the gas physical distances, these comparable resolutions potentially allow for an informative morphological comparison between dust extinction and HI emission structures.

We then apply the Histogram of Oriented Gradients (HOG) method (Soler et al. 2019) to the gas and dust cubes to identify spatial correlations between the two ISM tracers. This method is originally designed to characterise the similarities in the emission distribution based on gradient orientations. In this work, HOG analysis quantifies the morphological similarity between the 2D plane-of-the-sky distribution of the 3D dust extinction and HI emission. This is done by comparing distance channels (D_{dust} in pc) from dust map with velocity channels (V_{HI} in km s^{-1}) from HI data. A velocity channel map and a distance channel map are considered morphologically similar if their gradients are mainly parallel, and dissimilar if they

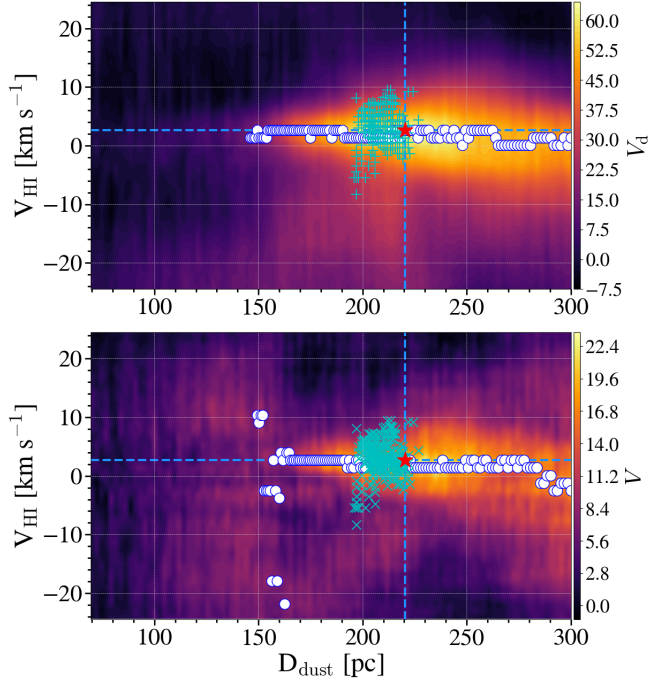


Figure A1. Morphological correlation between 3D dust distance channels and HI velocity channels for GASKAP’s Galactic Cirrus region $l = (270, 310)^\circ$, $b = (-45, -25)^\circ$. The correlation metrics are the direction-sensitive projected Rayleigh statistic (V_d in upper panel) and the projected Rayleigh statistic (V in lower panel). In both panels, circle markers indicate the velocity with the highest Rayleigh statistic values for each distance channel, star markers at the intersection of the dashed lines (at $D_{\text{dust}} = 220.3$ pc, $V_{\text{HI}} = 2.7 \text{ km s}^{-1}$) indicates the velocity-distance pairs with the highest Rayleigh statistic across all velocity and distance ranges. Plus markers (“+”) show velocity-distance matching from a simple matching between velocity at peak HI optical depth τ_{peak} and distance at peak dust extinction along 462 GASKAP lines of sight with HI absorption detections. Cross markers (“×”) show velocity-distance matching from a simple matching between velocity at peak HI brightness temperature $T_{\text{b},\text{peak}}$ and distance at peak dust extinction along the same HI absorption detection lines of sight.

exhibit randomly oriented. Specifically, for each pair of HI velocity and dust distance maps, the HOG method produces the projected Rayleigh statistic (V , see Soler et al. 2019) and the direction-sensitive projected Rayleigh statistic (V_d , see Soler et al. 2025) to quantify the relationship between the 3D dust and HI emission.

The Rayleigh statistic (V or V_d) assesses non-uniformity in a distribution of angles around a specific direction. A positive Rayleigh statistic indicates that the gradients are primarily parallel, signifying a morphological similarity between the HI emission and dust extinction in the corresponding velocity-distance channel pair. In contrast, a negative Rayleigh statistic suggests that the gradients are mostly antiparallel, leading to an anti-correlation between the dust extinction and HI emission intensities.

In this Section, we consider the local gas in the high galactic-latitude Cirrus region $l = (270, 310)^\circ$, $b = (-45, -25)^\circ$ with velocity range from -25 to $+25 \text{ km s}^{-1}$, and the dust distance from 69 to 300 pc from the Sun. Figure A1 illustrates the HOG morphological correlation between velocities from HI emission observations and distances from 3D dust extinction reconstruction for our region of interest. The upper panel displays the velocity-distance correlations with the direction-sensitive projected Rayleigh statistic V_d colour-

² The Hierarchical Equal Area isoLatitude Pixelization (Górski et al. 2005).

³ ZGR23 extinction curve: DOI 10.5281/zenodo.7811871

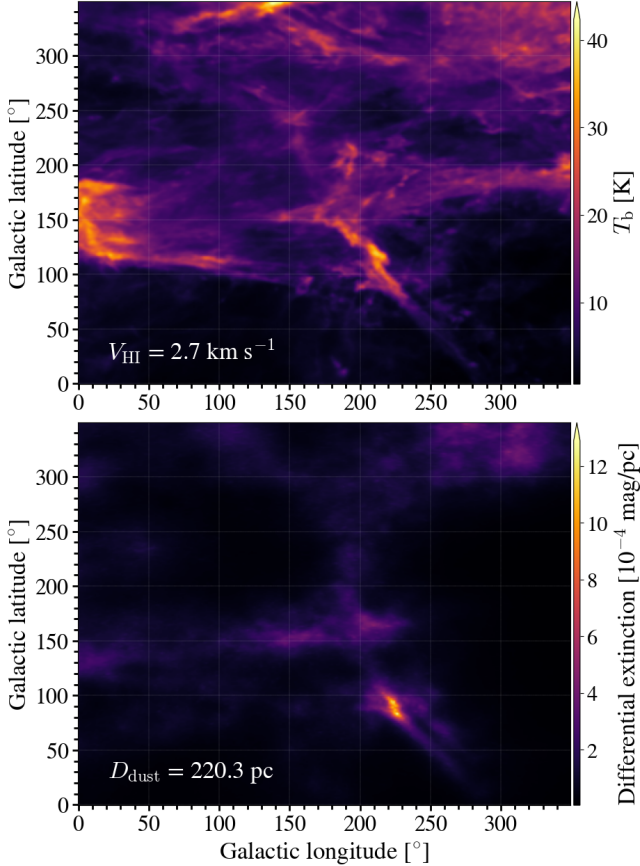


Figure A2. [Placeholder here, the axes are not correct! Juan is updating this!] H_I velocity and dust distance channels with highest morphological correlation. This example corresponds to the highest V_d (and V) in the comparison between the H_I emission and the 3D dust extinction presented in Figure A1. *Left:* HI4PI emission at velocity $V_{\text{HI}} \approx 2.7 \text{ km s}^{-1}$. *Right:* Dust differential extinction at distance $D_{\text{dust}} \approx 220.3 \text{ pc}$ obtained from Edenhofer et al. (2024).

coded, the lower panel for the same correlations but for the projected Rayleigh statistic V . Following Soler et al. (2025), V_d values at ~ 0 indicates a random orientation and low morphological correlation between the gradients of the two tracers. Values of $V_d > 2.87$ suggest mostly parallel gradients and a significant morphological correlation, whereas $0 < V_d < 2.87$ indicate mostly antiparallel gradients. Within each distance channel, white dots mark the velocity with the highest Rayleigh statistic values. Star markers denote the velocity-distance pairs with the highest Rayleigh statistic across all velocity and distance ranges. In both panels they are exactly at the same velocity-distance pairs $D_{\text{dust}} = 220.3 \text{ pc}$, and $V_{\text{HI}} = 2.7 \text{ km s}^{-1}$, although the white dots are more dispersed for the V Rayleigh statistic values, in particular at closer distances $D_{\text{dust}} < 170 \text{ pc}$.

Figure A2 presents an example of H_I emission along with dust extinction distribution, for the velocity-distance pair that obtains the highest morphological correlation as identified by the peak V_d and V values in Figure A1.

In addition to the HOG approach, we performed a simple velocity-distance matching. This involved comparing the velocity at peak H_I optical depth (τ_{peak}) with the distance at peak dust extinction along 462 GASKAP lines of sight with H_I absorption detections. We also matched the velocity at peak H_I brightness temperature ($T_{\text{b,peak}}$) with the distance at peak dust extinction along the same lines of

sight. These simple matchings are represented by plus (“+”) and cross (“×”) markers in the upper and lower panels of Figure A1, respectively.

Both HOG analysis and simple velocity-distance matching indicate that the distances to local H_I gas in the direction of the Magellanic Clouds range from 160 pc to 260 pc, with a likely distance $\sim 220 \text{ pc}$ and a corresponding H_I gas velocity of $\sim 3 \text{ km s}^{-1}$.

This paper has been typeset from a $\text{\TeX}/\text{\LaTeX}$ file prepared by the author.